HONG-YEE CHIU
NASA/Institute for Space Studies
New York, NY 10025
WILLIAM COLLINS
NASA/Institute for Space Studies
New York, NY 10025
and Columbia University
New York, NY 10027

A Spectroradiometer for Airborne Remote Sensing

Sensor design and calibration, and applications to geologic mapping of altered rock, to vegetation canopy studies, and to water body studies, are described.

ABSTRACT: *A parallel electro-optical input spectroradiometer system with 500 channels and operating in the 400-1100 nm wavelength region has been designed and fabricated for use in a light aircraft. The airborne system was conceived for determining the high-spectral-resolution properties of various ground targets of interest in remote sensing. Spectral radiance data at 4-digit resolution are generated on a 9-track tape in computer compatible format. At a survey altitude of 600 m and 200 km/hr ground speed, a ground resolution element is 18 meters square. The data acquisition rate is 2.5 spectra per second of 500 channels each. Absolute radiometric calibration is achieved with a standard lamp that is calibrated against an NBS secondary standard source. The linearity of instrument response to intensity change is 1 percent.*

The rapid data acquisition in parallel input channels is essential for obtaining good quality spectral data at 2 nm or better wavelength resolution and high sensitivity under airborne operating conditions. These data have yielded spectral information valuable to basic remote sensing research in the areas of detecting geologic zones of alteration, monitoring the condition of vegetation canopies, and determining the spectral properties of water bodies.

INTRODUCTION

IN RECENT YEARS remote sensing has become an important area of research in our endeavors to understand the nature and dynamics of our environment. Apart from the obvious military applications, remote sensing is beginning to make a significant contribution to the economics and well-being of mankind. The techniques of remote sensing in the visible and near-IR wavelength region vary greatly, but the general idea has been to obtain spatially correlated spectral information which, when coupled with other physical or chemical knowledge, will enable us to make qualitative or quantitative assessments of our environment.

Aerial photography (via film or vidicon camera systems) continues to be a major tool of passive remote sensing in the visible and near-IR region of the energy spectrum. Undeniably, photography offers certain advantages which can hardly be surpassed, such as the high spatial resolution, the relatively low cost of operation, and the enormous capacity to store large volumes of data. However, spectral resolution achievable from the direct usage of photography has been poor owing to the inherent wide spectral response of the photographic emulsions. Multi-channel aerial photography (with the help of bandpass filters) can to a certain extent amend these shortcomings. However, the equipment becomes complicated, cum-

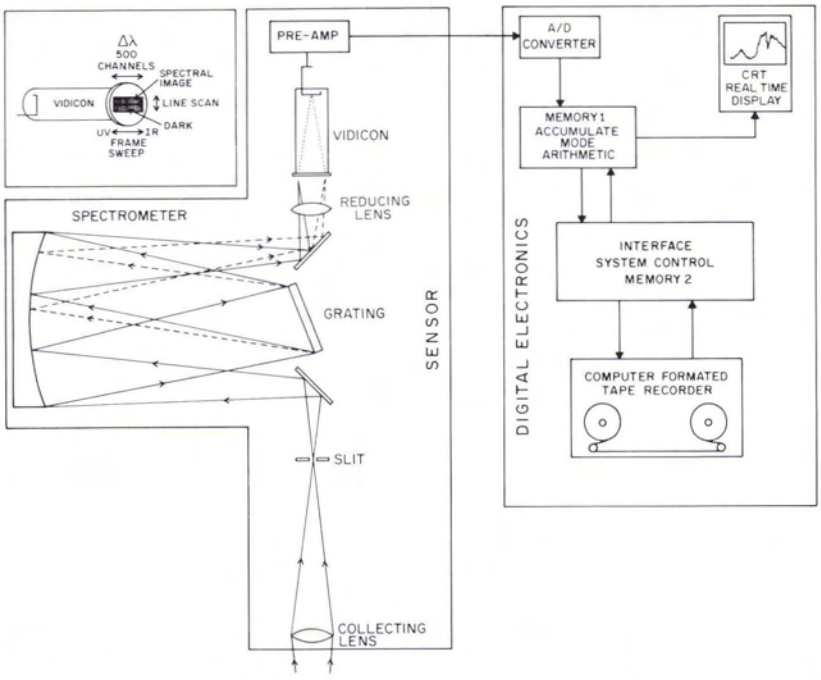

FIG. 1. Schematic diagram of the airborne instrument system. Radiation through the front optics is dispersed by the spectrometer and refocused on the vidicon. The vidicon raster format is shown in the inset diagram. Analog signals from the detector are sent to the electronics package for processing and recording.

bersome, and expensive when the number of channels exceeds four.

In order to supplement the information gap resulting from the low spectral resolution of aerial photography and satellite multi-channel spectral scanner and vidicon systems, the present airborne spectrometer system was developed by Columbia University with the support of Goddard Institute for Space Studies. Coupled with the requirement for extended area survey, the specifications that governed the design and fabrication of the spectroradiometer system were

(1) High spectral resolution,
(2) Portable and operable in a small aircraft,
(3) Real time data acquisition from a moving platform, with digital data storage, and
(4) No moving parts in the spectroradiometer proper (for accuracy and reliability).

These specifications were met or surpassed in the completed spectroradiometer system. This instrument has been flown for several years. Some research results are being published (Collins, 1977, 1978; Collins *et al.*, 1977). It is the intention of this paper to describe the principles and operations of this instrument in detail, and to review some of its present applications.

Design Concepts and Instrumentation

In view of requirements for high spectral resolution and parallel optical input, a spectrometer is used to disperse light collected by the fore optics. The optical dispersion unit in the present system is a Jarrel-Ash 0.33 meter Ebert spectrometer using all reflective optics. This design, with a 75 groves per mm grating, offers a compact package, fast optics (f:4.6), and proper spectral resolution for remote sensing applications. Radiance from the target is imaged on the entrance slit (Figure 1) by a 210 mm focal length, f:4.8 lens with an adjustable aperture to f:22.0. Radiation through the slit is collimated, dispersed by a grating, and refocused on the sensor array at the exit focal plane. At the exit end, an additional lens of 100 mm focal length is used to reduce the width of the spectrum to fit the vidicon sensor array format.

The vidicon in Figure 1 is the sensor of a commercially available instrument: the "Optical Multichannel Analyzer" (OMA) (Princeton Applied Research Corp., 1973). The OMA vidicon detector offers 500 channels of spatially resolved elements, each 25 μm by 2.5 mm. The 500-channel format is

derived from a 500-line TV raster scan; each line becomes a spatially resolved detector element. A slit image of chromatic light in a spectral channel of $\Delta\lambda$ width coincides with a raster scanning line 25 μm wide. The signals on the top half of a line (inset in Figure 1) are integrated along the line scan; the integrated image signal is the total incident energy from the target area in the interval $\Delta\lambda$ plus the dark current on the spatially resolved element. Dark current is read also on the lower half of the raster where no image is applied. This dark current is subtracted from the integrated image signal of each line scan. The line scan output is the "corrected" image intensity.

The 500 line TV raster frame is read out at a rate of 64 μsec per line (one spectral channel) and 32 milliseconds per frame (one 500-band spectrum). The output from each spectral channel is digitized and sent to one of the two internal memories, M1A and M1B, of the OMA. In the airborne operation, spectral data is summed in M1A where the sum of up to 10^4 scans can be stored. The data in M1A can be read out in analog format in real time and displayed on an oscilloscope; they are also made available in digital form for recording. Memory M1B is available to store amplifier bias current data or other spectra.

The photodiodes in a vidicon are storage devices responding to total energy incident between readouts. Time resolution between readouts is lost, but the spatial relations can be preserved according to the scan modes used. The output signal of the OMA detector electronics can be written as

$$S(x) = \int_0^T \int_{\Sigma_y,\,\Delta x} F(x,y,t)\,dt\,dy \ [\text{counts} \cdot \text{ch}^{-1}], \quad (1)$$

where $S(x)$ is the digitized detector signal at location x; $F(x, y, t)$ is the radiant flux at the spatial coordinates x, y on the detector surface. (Flight takes place in the x-direction while the slit is in the y-direction). T is the readout interval. The line scan integrates the total energy incident over the time interval between readouts, which is 32 msec, and it integrates over the chromatic image of the spectrograph entrance slit, which is focused on the 2.5 mm by 25 μm detector element. Spectral information is preserved in 500 intervals in Δx along the frame sweep but spatial variables in each chromatic image are integrated over the line scan area, Σ_y, Δx.

The vidicon system, functioning as a parallel input device, achieves considerable gain in sensitivity and simplicity of design over serial input devices using radiant flux detectors. Parallel optical input is the essential design element in the airborne application. It permits high spectral resolution measurements in 500 bands to be made in real time; equally important, the simple design offers reliable operation from a light, inexpensive aircraft.

The OMA is controlled by a hardwired controller of our own design and construction. This controller monitors and cycles the operation of the OMA and sensor while dumping the summed data into a computer formated 9-track magnetic tape recorder via a buffer memory (M2), which is part of the controller. The controller also monitors data going onto tape for errors, and it triggers a "ground truth" camera on every tenth spectrum going to tape. Table 1 correlates the time domain procedure with the data format. The entire system functions continuously and automatically along an aircraft flight line. A 9-inch tape (1200 ft) enables continuous recording for 20 minutes. One tape holds approximately 4,800 spectra in 500 bands with 4-digit resolution.

The instrument package consists of an electronics rack (0.5 meter wide, 0.6 meter deep, 1 meter high) and the sensor. Together they weigh about 110 kilograms. Power consumption is approximately 300 watts supplied by a 500 watt inverter. The system is flown in a light aircraft, nominally 610 meters above the terrain with the sensor looking vertically at the ground along the flight path. The instantaneous field of view is 18 meters by 2 meters at this height (Figure 2). This shape is determined by the rectangular dimensions of the spectrometer entrance slit. The long axis of the field of view is fixed perpendicular to the flight direction. Ten spectra, or frame sweeps, are summed over 0.32 seconds corresponding to 18 meters of aircraft motion along the ground track. The sum of ten frame sweeps is recorded on tape and later averaged to obtain the spectral response integrated over an 18 meter square field of view. In the cycle of adding ten frames—dump to tape—start new summation, three frames are skipped. Blocks of data on tape in 500 spectral bands correspond to consecutive 18 meter square integrated target areas along the flight path with about 3 meters spacing between. "Ground

TABLE 1. FLOW DIAGRAM OF THE AIRBORNE INSTRUMENT INTERNALLY PROGRAMMED OPERATION. THE OPERATOR GIVES THE START SIGNAL AT THE BEGINNING OF A FLIGHT LINE AND THE SEQUENCE OF EVENTS AND TIMING ARE CARRIED OUT WITH AUTOMATIC RECYCLING UNTIL THE OPERATOR GIVES THE STOP SIGNAL.

Time Domain	Procedure	Data Material
64 μsec.	vertically scan one channel	one 1.396-nm wide spectral channel
32 msec.	sweep one vidicon frame of 500 channels	one spectrum to memory MIA
320 msec.	sum up 10 frames in memory MIA	one averaged spectrum
3 × 32 msec.	memory MIA data IBM formatted and recorded on tape	one averaged spectrum on tape

truth" photographs taken every tenth dump to tape have about 60 percent overlap.

CHARACTERISTICS OF THE SILICON VIDICON SENSOR

The silicon target of the vidicon is a microscopic matrix of photodiodes made from Si p-n junctions spaced 8 μm between centers. The diodes are biased at a voltage somewhat less than 10 volts. An electron beam of ≈25 μm diameter scans the target in a raster pattern and deposits electrons onto the target until the target potential equals that of the thermionic cathode, where the electron beam originates. Incoming photons discharge the diodes forming a charge image. The charge image will be retained until discharged by leakage or by the scanning electron beam. The scanning electron beam replenishes the charge in depleted regions in proportion to the amount depleted by incoming photons. The deposition of charge causes an induced e.m.f. in the target electrodes in proportion to the integrated intensity of light. This induced e.m.f. is the video signal.

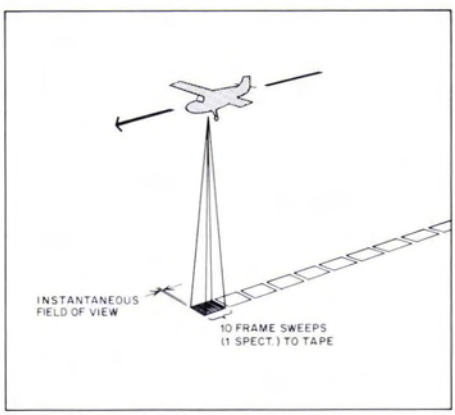

FIG. 2. Survey procedure. Spectral measurements are integrated over consecutive 18 m square areas along the ground track and recorded. Flight lines are arranged to cross targets of interest.

The silicon diode operates through an energy gap ≈0.6 eV; photons with energy greater than 0.6 eV can in principle cause the diodes to discharge. However, as the transparency of silicon increases toward longer wavelengths, the useful sensitivity ends somewhere around 1,100 nm. For wavelengths shorter than 400 nm, radiation does not penetrate the surface far enough to discharge the diodes. The useful sensitivity lies between 400 nm and 1,100 nm.

In the wavelength regions between 500 nm and 900 nm, the quantum efficiency, E_q, of the silicon diodes is quite high, around 80 percent or better. Each photon discharges E_q electrons in the diode, whose charge holding capacity is $\approx 10^6$ electrons. The ability to detect photons is thus governed by the sensitivity of the pre-amplifier. The best preamplifier can detect 100 electrons but such sensitive pre-amplifiers have a rather limited bandwidth (less than 50 kHz). For operations in the OMA mode, the pre-amplifier noise is around several thousand electrons. This means that in each pixel several thousand photons must be accumulated before the signal is perceivable above noise level. This is, however, not a serious problem in most remote sensing applications since more than enough light is usually available.

The operation of the silicon vidicon is plagued by several fundamental physical problems, which can limit its performance as a spectroradiometer detector. These problems have been well studied in low light level astronomical research (McCord and Westphal, 1972; McCord and Frankston, 1975; Westphal *et al.*, 1975; Hunten *et al.*, 1976). The vidicon problems are:

(1) Moiré pattern. The diodes in the silicon target are arranged in geometrically accurate arrays. The scanning raster pattern is a set of closely packed parallel lines, slightly distorted from the straight line due to many factors associated with deflection mechanisms. The imposition of a scanning raster

upon a geometrically accurate diode array pattern will introduce a Moiré pattern.

This problem is considerably reduced in the OMA design because the entire video scan line in the OMA is summed to give a single output characterizing the total light falling onto a large number of diode elements along the vertical raster line. This mode of operation also reduces the effects of nonuniformities in photo-sensitivity across the target plate.

(2) Beam landing uncertainty. Because of their thermionic origin, electrons in the vidicon electron beam have an exponential energy distribution with a spread on the order of kT, where T ≈ 1000°K, the resulting energy spread is a small fraction of eV. Thus, even in a properly charged (unexposed) target, some super energetic electrons can always land; while in a strongly depleted region (heavily exposed) the replenishment of charge cannot be complete in one passage of the beam, because portions of electrons having less energy are repelled even though the charging process is not completed. In the next scan, an electron beam will tend to land in a previously heavily exposed area, giving the effect of a residual image. This phenomenon is known as "lag."

A number of studies have been made to reduce the lag. It is found that for a silicon target, the ratio of the residual image to the original image in terms of currents, I_r, I_o, that would have been required to completely replenish the charges (Logan and Watton, 1972), is

$$\frac{I_r}{I_o} = e^{bV_e} \qquad (2)$$

where V_e is the cathode potential, which is between −0.5 to −1 volt, and b is of the order of 3-5 v^{-1} (Hunten *et al.*, 1976). Although Equation 2 is correct in certain regions, there is some discrepancy, which is probably due to the simplified model used to derive it. Our measured value of I_r/I_o is ≈0.17 for the present vidicon spectroradiometer system.

(3) The "beam pulling" effect. A strongly depleted region, having a high potential, can distort the trajectory of the electron beam as it approaches the target with a near zero velocity. An electron beam scanning near a heavily depleted (heavily exposed) region can, therefore, be pulled from its designated trajectory to land on an adjacent site, thus causing an apparent shift of the line scan. In the worst case, a line scan may be caused to shift by as much as one spectral channel. This can cause an apparent shift of spectral lines.

(4) Dark current. Even perfect diodes exhibit some leakage, which is caused by energetic components of thermal motion in electrons that manage to cross to the conductance band. In a 32 msec raster, the dark current is in the range of several percent of the saturation signal. The dark current may be reduced by cooling. The dark current effect is reduced in the OMA system by subtracting the lower half of the line scan as described earlier.

In summary, a silicon vidicon has the merit of a broad spectral response to include the near IR, its operational procedures are well practiced and known, and devices are commercially available and relatively inexpensive. However, it is plagued by two fundamental problems which are yet to be solved, at least in fast data fetching operations. These are the residual image problem (lag) and the beam pulling phenomenon. The lag problem is particularly serious when one makes a transition from a bright scene to a relatively dim one. The beam pulling phenomenon will deteriorate spectral resolution.

Instrument Calibration

Aircraft spectral measurements in 500 channels per spectrum are calibrated to convert recorded digital data from the instrument in counts per channel to apparent radiance (radiance received at the entrance aperture) per wavelength interval. Calibration measurements are made in the laboratory before the instrument is installed on the aircraft for a series of survey flights and again after it returns. The absolute calibration relates aircraft measurements to the radiance of a standard lamp. One calibration is applied to all measurements in a single flight line in order to preserve the separation of inherent inaccuracies in the absolute calibration from the precision of relative measurements along the flight line. Precision among spectral measurements in a flight line is affected by error in wavelength-channel correlation (caused by drift in grating position due to mechanical and temperature induced strain), drift in sensor electronics and detector sensitivity (mainly a function of temperature variation), and microphonics in the optical system. The drift due to temperature variations is small over a flight line of 2 to 3 minutes' duration, and optical noise is controlled by careful design and construc-

tion. The precision over a flight line has a much closer tolerance than the accuracy of absolute calibrations. The absolute calibrations will be affected by those factors affecting the precision, only over much greater time periods and ranges in temperature. The absolute calibration is also dependent on the accuracy and precision of the calibration source.

The signal output of the instrument can be broken down, disregarding the radiation-field effects, as functions of the mean spectral radiance of the target, and of the instrument factors. Radiant energy through the system is affected by the optical properties of each component in the collecting optics and the dispersing device before it reaches the detector element. At the detector, the efficiency of the photon to electric signal conversion is a function of wavelength, position on the detector surface, and angel from the normal of incident radiation. The analog electronic signal produced at the detector is processed through several stages of amplification, in each of which amplifier gains modify the signal before it is digitized. All of the instrument factors combined determine the radiance responsivity, R_N, of the total system at the time of the measurement. The amplified and digitized output signal, S_I, of the instrument can be written

$$S_I = \int_{\Delta\lambda} \bar{N}_\lambda(\lambda)\, R_N(\lambda)\, d\lambda \,[\text{counts}] \qquad (3)$$

for each channel of a spectral measurement. The mean spectral radiance, $\bar{N}_\lambda$, is the signal at the entrance aperture, which is spatially integrated over the instrument field-of-view.

The spectral response of each instrument component can be assumed constant over the narrow wavelength, $\Delta\lambda$, of an instrument channel. The ouput signal by a channel can be written in simplified form with all instrument parameters included:

$$S_I = \bar{N}_\lambda\, T\, \tau_O\, \tau_F\, E_G\, R_D\, \Delta\lambda \,[\text{counts}] \qquad (4)$$

The throughput, T, includes the geometric factors that determine the solid angle field-of-view, and the effective area of the entrance aperture. Included in T is the f-stop, or aperture stop, setting of the collecting optics used during the field observation. The transmittance of the optical train, τ_O, includes all lenses, mirrors, and the detector window. Spectral transmission properties of all filters used for each observation are in the filter factor, τ_F. The grating factor includes E_G, the spectral efficiency of the grating for non-polarized light. The detector response, R_D, is strongly dependent on wavelength, spatial distribution, and angle of incidence. To compensate for this, the grating is set with a frequency standard to position the spectrum on the vidicon detector as it was in the field measurement.

An instrument transfer function can be defined for each specific optical configuration:

$$C_\lambda = \left[T\, \tau_O\, \tau_F\, E_G\, R_D\, \Delta\lambda\right]^{-1} \left[\text{counts} \cdot \text{w}^{-1} \cdot \text{cm}^2 \cdot \text{sr} \cdot \text{ch.}\right]. \qquad (5)$$

A set of instrument functions for each of the 500 channels is calculated for every combination of f-stop, filters, and grating position used in the field observations. The instrument function can be calculated from Equation 4:

$$C_\lambda = \bar{N}_{\lambda_L} / S_I \left[\text{counts} \cdot \text{w}^{-1} \cdot \text{cm}^2 \cdot \text{sr} \cdot \text{ch.}\right], \qquad (6)$$

where $\bar{N}_{\lambda_L}$ is the mean spectral radiance of a white diffusing plate irradiated by a calibration lamp of known radiant intensity. Field measurements are calibrated from

$$N'_\lambda = S_T\, C_\lambda \left[\text{w} \cdot \text{cm}^{-2} \cdot \text{sr}^{-1} \cdot \text{ch.}^{-1}\right], \qquad (7)$$

where N'_λ is the apparent mean spectral radiance of a target, S_T is the recorded signal for the target, and C_λ is the channel by channel transfer function for the specific instrumental configuration. The spectral curves for the lamp measurement, the transfer functions, and the resultant calibrated lamp spectrum calculated from Equation 7 are shown in Figure 3. The baseline (amplifier bias) has been subtracted from the curves.

Frequency calibration is accomplished using a krypton emission line spectral lamp (Figure 4). The peaks of known wavelength can be located within 0.2 channels on the instrument display scope in real time. The channel width is calculated from the number of channels between the various peaks. The channel width, 1.396 ± 0.0025 nm, is a function of the grating dispersion and the spectrometer focal length. The 75 groves per millimeter grating disperses the interval from 400 nm to 1100 nm over 12.5 mm at 0.1 meter focal length. A split filter is placed in front of the detector to eliminate second order effects between 700 nm and 1100 nm. The low dispersion grating gives a very even wavelength distribution across the detector.

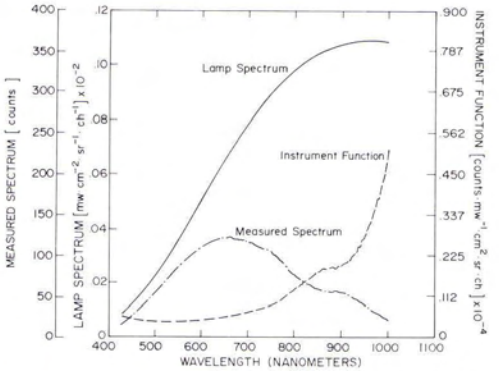

FIG. 3. True spectral curve of the ISCO calibration lamp (solid line) calculated from the instrument measurements and theoretical considerations. The instrument function was determined from a measured spectrum of the calibration lamp and from the known lamp spectrum.

Error translated to the end channels due to uneven dispersion is 0.625 nm, less than half a channel. Frequency alignment is made by positioning the 760.1 nm krypton peak on channel 250. Field calibration for grating setting is obtained from the position of the atmospheric oxygen absorption band centered at 760.5 nm. This absorption band is inherent in every field spectrum (Figure 6), allowing accurate monitoring of wavelength setting in the field data.

The field-of-view was mapped by using a light source through a small aperture at 200 feet from the sensor. It is 15 milliradians in the long slit dimension and 1.5 milliradians in the slit width direction. The system linearity with change in intensity measures ±1 percent using calibrated neutral density filters and the calibration lamp. The detector and amplifier rms noise, looking at a series of recorded reference baselines (front lens covered), is less than ±1 count in the scanning mode used. Most target measurement signals are between 100 and 700 counts per scan. The signal-to-noise ratio is greater than 100:1 in most cases. The maximum dynamic range is 750. The lag in response to signal change was measured by opening and closing the aperture while looking at a strong light source. The signal rises to 12 percent of the maximum in the first recorded spectrum on opening the lens, and the signal drops to 17 percent of the last signal on closing off the front lens ($I_r/I_o = 0.17$). The slow response time must be considered in planning flight lines and interpreting the data.

The maximum spectral standard deviation recorded for calibration measurements made before and after aircraft flights is 5.5 percent. The apparent drift in sensitivity can be traced mainly to temperature effects and frequency misalignment among measurements. The maximum standard deviation in sensitivity between the normal operating ranges of 60°F to 80°F is ±3.5 percent in the blue spectral region (Figure 5). There is a possible ±1 channel error in reproducing the grating settings as they were in the field. The oxygen absorption band is checked in every flight line, and wavelength drift is always less than 1 channel. This amount of frequency shift can cause up to 2.5 percent standard deviation in the spectral measure-

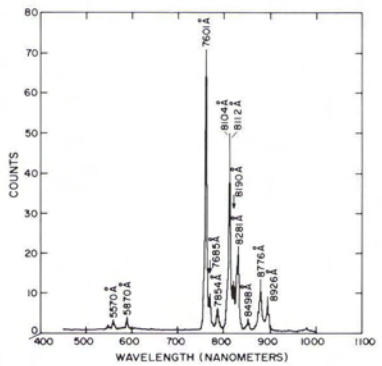

FIG. 4. Emission lines of a Krypton gas lamp. Location and spacing of the lines of precisely known frequencies are used in determining the instrument channel width and wavelength scale.

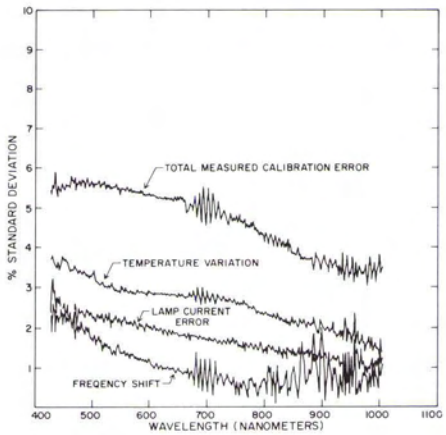

FIG. 5. Percent standard deviation as a function of wavelength among all before and after flight calibration lamp measurements. The three lower curves indicate measurement variation as temperature, frequency setting, and lamp current were varied under controlled laboratory conditions. The noise at 700 nm is the edge effect of the split filter for eliminating second order overlap.

ments. There is a possible error of the same amount due to lamp current adjustment error. The other sources of error, calibration lamp aging and electronics drift, have not been monitored.

The precision among all data collected is on the order of the error discussed above. Drift in sensitivity over lamp measurements of 2 to 5 minutes is less than ±1 percent. This should also be the precision of the data within a flight line. Most of the error in the relative calibrations would be removed by on board calibration. The accuracy, or absolute calibration, has the added error of the calibrated light source. The manufacturer's estimate on that unit is ±5 to 10 percent (Instrumentation Specialities Company, Inc.) relative to the NBS standard.

System Applications

Extensive data have been gathered with the airborne spectroradiometer instrument over several general types of remote sensing targets. Some examples of current applications are given in the following paragraphs.

Geologic mapping of altered rock

The high-spectral resolution instrument has been used to make a detailed airborne spectral study of hydrothermal alteration products in the Gold field, Nevada, mining district. With the airborne spectroradiometer technique, it is possible to make high-spectral-resolution field measurements of natural geolgoical targets over extended fields-of-view and from a remote vertical angle. Combined with the simultaneously acquired 35 mm photography of the ground track, measurement targets can be located precisely for correlation with "ground truth" data. Rapid spectral measurement of many target types along the flight path (background geologic terrain; limonite, hematitic, and jarosite rich zones; vegetated and heavily shadowed areas; etc.) permits analysis of the differential spectral properties among the targets to be discriminated. The high-spectral-resolution data also allow computer simulation of broader band instrument responses to these targets, including simulation of the spectral responsivity in the four bands of the Landsat multispectral scanner instrument. The band simulation technique was used to determine, from the aircraft data, the spectral differences among geologic targets in the Goldfield region as they appear to the Landsat system. This study has led to a deterministic computer method of discriminating among and mapping geologic targets using Landsat data (Collins, 1976, 1977).

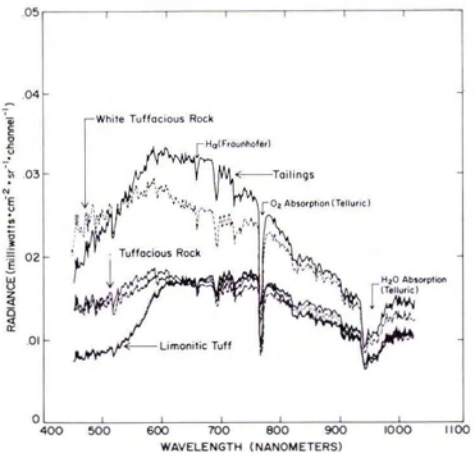

FIG. 6. Selected aircraft spectra from a geological survey in Goldfield, Nevada. The spectra are plotted in full instrument wavelength resolution. The high frequency variations in the spectral curves are caused by gaseous absorption in the Earth's atmosphere and groups of Fraunhofer absorption bands in the solar atmosphere.

Some individual spectra from the Goldfield survey are shown in Figure 6. Hydrated ferric iron minerals (limonite), hematite, and jarosite are characteristic of the altered zones, which are generally favorable for heavy metal deposits. The ferric iron absorption edge between 450 nm and 600 nm appears very strongly in the spectra from target areas rich in ferric iron minerals—limonitic tuff and tailings (high in jarosite). The characteristic broad ferric iron absorption band centered at ≈900 nm, however, appears surprisingly weak and variable in the aircraft spectra from Goldfield, except in the jarosite rich tailings, where it is quite strong. Subsequent studies indicate that the depth of the 900 nm absorption feature may be a function of mineralogy and surface concentration of the ferric iron minerals.

The aircraft data also indicate that remote discrimination and separation of the three main ferric iron minerals, based on the shape of the ferric iron absorption edge between 450 nm and 600 nm, should be possible under high spectral resolution. The shape of this absorption feature shown in Figure 6 is distinctly different for the limonite rich tuff and the jarosite rich tailings. The absorption edge of hematite was observed separately in laboratory samples. The shape of the absorption edge is similar to that of limonitic minerals; however, it advances farther into the longer wavelength region by

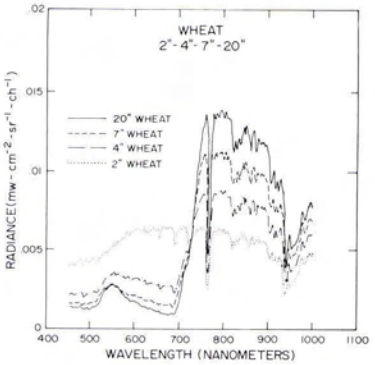

FIG. 7. Spectra of green wheat at various stages of growth as indicated. Spectral development is due to both plant maturation and increasing canopy density. These two effects can be separated under high resolution spectroscopy by a pronounced shift that occurs on the absorption edge between 700 nm and 750 nm during wheat heading.

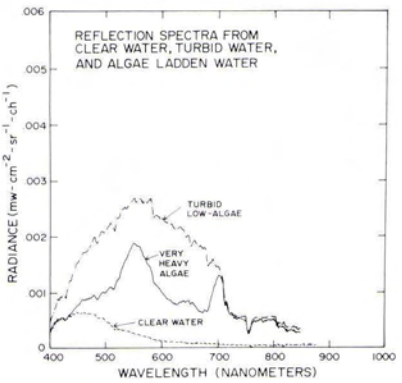

FIG. 8. Reflection spectra from clear water, turbid water, and algae-ladden water. Distinctive changes in the spectrum result from the algae content.

up to 50 nm. An airborne technique for identifying limonite rich hydrothermally altered zones, in contrast to hematitic sediments, would be an important exploration tool, and one that could be used in conjunction with Landsat mapping of high ferric iron zones.

VEGETATION CANOPY STUDIES

The spectral range and resolution of this system together with the advantages of the airborne technique as discussed above make it ideal for vegetation analysis. Many kinds of canopies have been studied; one of the most significant developments has come out of agricultural crop studies. The reflected spectral radiance curves of young wheat in several stages of growth are shown in Figure 7. The spectral development is due to both plant maturation and to increasing canopy density; the two effects cannot be separated by the broadband spectral features alone. It can be shown, however, that a far-red shift in the position of the chlorophyll absorption edge between 700 nm and 750 nm is characteristic of plant and pigment system maturation (Collins, 1978). This shift, visible only under spectral resolution of 2 nm to 10 nm, can be distinguished even under moderate variations in canopy density. A very pronounced red-shift occurs in the wheat spectrum at heading. This spectral shift and information in other spectral regions may enable wheat classification, canopy density evaluation, and grain yield estimation. Studies in progress also indicate that the position of the absorption edge shifts toward the blue end of the spectrum under stress conditions in forest species growing over sulfide mineral deposits (Collins *et al.*, 1977).

WATER BODY STUDIES

The spectral range and resolution of the system also make it ideal for remote sensing of water bodies. Reflected spectral radiance measurements taken over two lakes, Lake Tahoe and Clear Lake in California, are shown in Figure 8. The small rise in the blue region of the Lake Tahoe spectrum is due to short wavelength scattering in the sediment and algae-free water. The two spectra from Clear Lake show the reflected radiance of highly turbid water and the superimposed absorption by algae pigments.

A three-dimensional plot of algae-laden water in Clear Lake is shown in Figure 9. Three different physical domains are represented in the three dimensions: ground track (space)along the x-axis, spectral wavelength (frequency) along the y-axis, and spectral radiance (energy) in the z-axis direction. Blue-green and red absorption and green reflection vary smoothly, indicating increasing pigment absorption along the flight path from right to left. The far red reflection peak, however, behaves erratically. This peak occurs in the narrow zone between pigment absorption in the red region and water absorption in the far-red and near-infrared. The fluctuation in the narrow red reflection peak may be due to the depth distribution of the algae, especially in the near surface layers of water.

DISCUSSION

The advantages of the airborne spectroradiometer system developed at Colum-

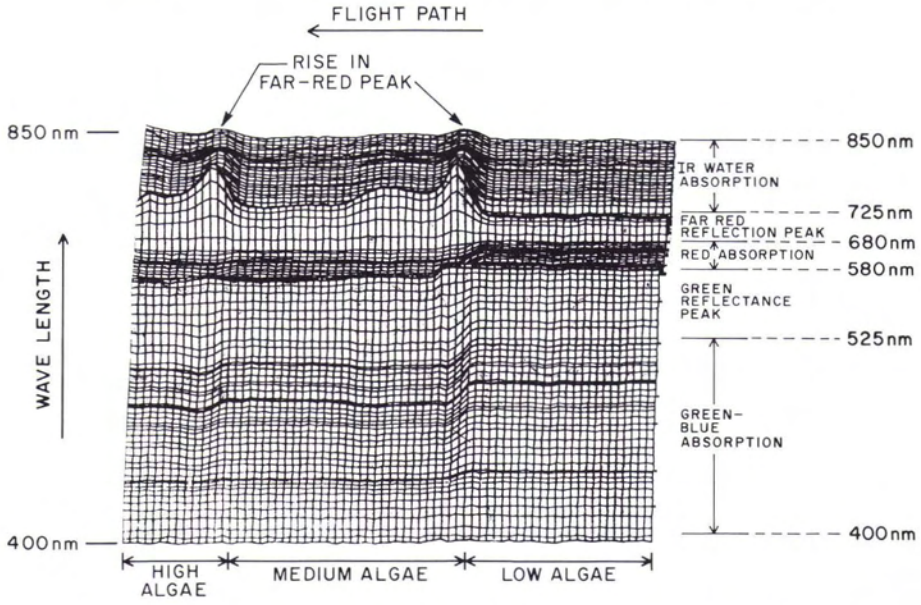

FIG. 9. Three-dimensional plot of algae-laden water in Clear Lake, California.

bia University lie in the high-spectral-resolution with parallel electro-optical input, the airborne data gathering technique, the ease and reliability of operation, and the facility and speed of processing computer-compatible tapes. The system sensitivity is more than adequate to obtain useful quantitative results under daylight illumination and at data aquisition rates compatible with the airborne operating requirements. The current system, ruggedized for aircraft flight, is relatively trouble free, and no major repair was needed during its four years of operation.

The airborne system has been used to observe natural extended targets and to detect subtle spectral features not visible to other lower wavelength resolution instruments. With high spectral resolution in 500 bands, it is possible to apply sensitive waveform analysis techniques, and to obtain derivative spectral curves, for determining subtle changes in the shapes and positions of spectral absorption bands. The 500 band data is also amenable to broader-band simulation analysis. The band simulation technique has been used to evaluate broad-band system spectral responsivities to natural targets, and to empirically determine and test optimum optical configurations for broad-band systems. Along with determining the spectral characteristics of targets to be discriminated, the airborne system has been used to determine the nature and magnitude of spectral variations among the natural background targets in a survey area. The background "noise" variation problem is a critical consideration in multispectral survey data analysis.

Research with the airborne spectroradiometer system has lead to the discovery of a method to determine agricultural crop type and plant condition based on the physicochemical states of the pigment systems. The same method, of observing the position and shape of the chlorophyll absorption edge under high spectral resolution, has been applied to detecting plant stress over zones of sulfide mineralization. The band-simulation and other techniques described have been employed in devising a successful computerized method for mapping exposed geologic zones of alteration and possible heavy metal mineralization using Landsat data. The airborne system has also found important application in observing subtle spectral features of water bodies. The spectral information in water spectra, once understood and quantified, could open the way to reconnaissance and water quality management not possible under present slow and tedious ground based methods.

The need clearly exists for high-spectral-resolution airborne survey instruments in remote sensing applications. The prototype vidicon system presented here has helped to open the way toward this field of research. However, faster, compact, and more versatile solid-state detector systems will probably be the key to future high-spectral-resolution research and applications in re-

mote sensing. Though these solid-state airborne survey systems are not available commercially, their construction is within present technological capabilities. Current research plans at Columbia University include construction of a linear solid-state array system that would extend the range of spectral sensitivity farther into the infrared, and construction of a two-dimensional array system that would enable two-dimensional ground coverage.

ACKNOWLEDGMENTS

This research was supported by a grant to Columbia University from NASA, Institute for Space Studies, Goddard Institute for Space Studies, Goddard Space Flight Center. We are grateful to Prof. Peter Ypma, The University of Adelaide, Australia, who established this remote sensing project at Columbia University.

REFERENCES

Collins, W., 1976, *Spectroradiometric Detection and Mapping of Areas Enriched in Ferric Iron Materials Using Airborne and Orbiting Instruments*, Ph.D. Thesis, Columbia Univ.

———, 1977, "Airborne Spectroradiometer Analysis and LANDSAT mapping of Hydrothermal Alteration", *Geophysics* (in press).

———, 1978, "Identification of Crop Type and Maturity Using High Resolution Spectral Features in the Near Infrared", *Photogrammetric Engineering and Remote Sensing* 44, 43.

Collins, W., Gary L. Raines, and Frank C. Canney, 1977, "Airborne Spectroradiometer Discrimination of Vegetation Anomalies Over Sulfide Mineralization—A Remote Sensing Technique", Geological Society of America, 1977 Annual Meeting, Abstracts with Programs.

Instrumentation Specialties Company, Inc., nd., *Instrumentation Manual—Model SRC Spectroradiometer Calibrator*, Instrument Specialties Company, Inc., Lincoln, Neb.

Hunten, D. M., and C. J. Stump, Jr., 1976, "Performance of a Silicon Vidicon at Low-Light Levels", *Applied Optics 15*, 3105.

Logan, R. M., and R. Watton, 1972, "Analysis of Cathode Potential Stabilization of the Pyroelectric Vidicon", *Infrared Phys. 12*, 17.

McCord, T. B., and M. J. Frankston, 1975, "Silicon Diode Array Vidicons at the Telescope: Observational Experience," *Applied Optics 14*, 1437.

McCord, T. B., and J. A. Westphal, 1972, "Two Dimensional Silicon Vidicon Astronomical Photometer", *Applied Optics 11*, 522.

Princeton Applied Research Corp., 1975, *Optical Multichannel Analyzer (OMA), Operating and Service Manual*, Princeton Applied Research Corp., Princeton, New Jersey.

Westphal, J. A., J. Kristian, and A. Sandege, 1975, "Absorption-line Redshifts of Galaxies in Remote Cluster Obtained with a Sky-Subtraction Spectrograph Using a SIT Television Detector", *Astrophysical Jour. Letters 197*, L95.

Errata

In the article, "Land Use Map Accuracy Criteria," by R. Michael Hord and William Brooner in the May 1976 issue, Table 1 (page 673) contains the following misprints: The lower limit for $N = 50$ and $\bar{x} = 80$ appears as 0.6896 and should read 0.6696; the lower limit for $N = 50$ and $\bar{x} = 85$ appears as 0.7624 and should read 0.7264; and the lower limit for $N = 50$ and $\bar{x} = 95$ appears as 0.3514 and should read 0.8514.